Asian Journal of Chemistry; Vol. 37, No. 8 (2025), 1965-1974

ASIAN JOURNAL OF CHEMISTRY

https://doi.org/10.14233/ajchem.2025.34081

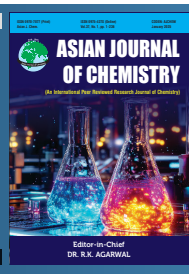

Synthesis, Crystal Structure, DFT, TD-DFT and DOS Analysis of *Bis*-[2-(3-hydroxy-4-methoxyphenyl)-4,5-diphenyl-1*H*-imidazol-3-ium]oxalate Ethanol Solvate

PETER SOLO[1,2,*], M. AROCKIA DOSS[3,4], MICHAEL PILLAY[5] and THARSIUS RAJA WILLIAM RAJA[5]

[1]Department of Chemistry, St. Joseph's College (A), Jakhama-797006, India
[2]Department of Environmental Studies, St. Xavier College, Jalukie-797110, India
[3]Department of Chemistry, St. Joseph University, Chümoukedima-797115, India
[4]School of Science and Humanities, Emmanuel Educity, Tindivanam-604307, India
[5]Department of Life and Consumer Sciences, College of Agriculture and Environmental Sciences, Florida Campus, University of South Africa, Johannesburg 1709, South Africa

*Corresponding author: E-mail: solopeter82@gmail.com

Received: 19 May 2025; *Accepted*: 10 July 2025; *Published online*: 31 July 2025; AJC-22075

A novel imidazolium-oxalate co-crystal was synthesized and characterized using spectroscopic method and single-crystal X-ray diffraction studies. The compound crystallizes into triclinic space group ($P\bar{1}$) with a = 8.792(3), b = 10.814(4), c = 13.024(5), α = 82.881(9), β = 75.347(9), γ = 67.811(9), a volume of V = 1108.7(7) Å^3 and Z = 1. The X-ray diffraction studies confirms deprotonation of both the protons from oxalic acid and the protonation of pyrimidine-type nitrogen of the imidazole ring. The crystal structure is largely stabilized by the existence of N–H···O and O–H···O polar interactions between the protonated imidazole compounds and the oxalate ions. Density functional theory (DFT) calculations demonstrated a strong correlation between the optimized constrained structure and the experimental findings. UV-visible spectroscopy, time dependent-DFT and density of states (DOS) studies were performed to study the optical and electronic properties of the studied crystal. With a band gap of 1.807 eV, the organic crystal can be investigated for its applications in organic semiconductors and optical materials.

Keywords: Imidazolium-oxalate, Single crystal XRD, Hirshfeld surface, DFT, TD-DFT, DOS.

INTRODUCTION

Organic crystals are largely investigated for their properties in optoelectronic [1], photonics [2-5], chemical sensing [6,7], explosives [8,9], gas storage [10-12], dyes and pigments [13, 14], drug delivery [15] and as linkers in MOF [16-18]. Imidazole with its unique ability to act both as an acid and a base, forms diverse polar interactions which are crucial solid structures [19]. Numerous imidazole-based organic crystals [20-22] are known, including benzimidazoles [23-25] and phenanthroimidazoles [26-28]. Imidazole and its derivatives are being investigated for organic semiconductor applications due to their unique properties, structural versatility and ability to form ordered crystalline or thin-film architectures. Their aromaticity, π-conjugation and hydrogen-bonding capacity make them promising candidates for charge transport materials in organic electronics [29-32]. Thieno-imidazole based small molecule has been applied as hole transport materials in perovskite solar cells [33]. Imidazolium salts have been studied for improving the efficiency and stability of perovskite solar cells [34,35]. Benzimidazole derivatives have been investigated as n-type semiconducting materials [36]. Phenanthroimidazole-iridinium complexes have been studied as light-emitting electrochemical cells [37]. The group has also synthesized several phenanthroimidazole crystals and have investigated their charge transport properties [38-40].

Thus far, only a few imidazolium-oxalate co-crystals have been known [41-43]. Like our previous study [38], we introduce a new imidazolium-oxalate co-crystal, whose structure has been confirmed with spectroscopic and single crystal XRD studies. Extensive computational tools were utilized to study its structure and electronic properties. UV-Visible spectroscopy combined with TD-DFT and density of states (DOS) studies have also been performed to understand its electronic excitation and prediction of band gap, which are crucial for the study of organic semiconductor and optical materials.

EXPERIMENTAL

Synthesis and crystal structure: The reactions scheme for the synthesis of single crystals of the studied compound is shown in **Scheme-I**. Imidazole derivative (**4**), was synthesized through a one-pot condensation reaction involving benzil (4.205 g, 20 mmol) (**2**), 3-hydroxy-4-methoxybenzaldehyde (3.043 g, 20 mmol) (**1**) and ammonium acetate (4.625 g, 60 mmol) (**3**), using ceric ammonium nitrate (CAN, 0.054 g, 1 mmol) as a catalyst [44]. The mixture was subjected to reflux in ethanol for approximately 4 h, with progress monitored with TLC. Following the reaction, the mixture was poured into ice-cold water and the resulting precipitate was purified through recrystallization in 90% ethanol. Imidazolium-oxalate co-crystals (**5**) were subsequently obtained by heating the imidazole derivative (**4**) with equimolar amounts of oxalic acid in ethanol and slowly cooling the solution.

Characterization: The analysis of the FT-IR spectra for the compound was conducted in the range of 3500-500 cm^{-1} utilizing a Bruker FTIR ALPHA instrument with KBr in pellet form. The ^1H NMR and ^{13}C NMR spectra were acquired on a BRUKER AVANCE III 400 instrument, operating at 400 MHz and 100 MHz, respectively. The UV-Visible spectroscopy was recorded using a UV-2600i instrument, employing ethanol as solvent.

Crystal structure analysis: The collection of XRD data was performed using a BRUKER APEX-II CCD diffractometer with Mo*K*α radiation. The solution and refinement for the crystal structure were performed with SHELXS [45] and SHELXL [46] program, respectively using Olex2 program [47].

Computational analysis using density functional theory: DFT studies were executed on a computer system that has 24 cores, utilizing the computational chemistry software package Gaussian [48]. Frozen phase optimization using DFT/B3LYP functionals with 6-311G(d,p) basis sets were performed on the crystal structure, where the surrounding molecules were frozen, allowing only the molecules of interest to be optimized. For normal optimization, diffusion functions were added to the basis sets. Molecular electrostatic potential and HOMO-LUMO studies were performed from these optimizations. Root mean square deviation and R^2 correlation were calculated to compare the theoretical structure with the experimental structure [39]. CrystalExplorer was used to analyzed intermolecular interactions and packing in the crystal system [49]. TD-DFT studies were performed in solvent phase (ethanol) using polarizable continuum model for the SCRF method [50]. Band gap and DOS (density of states) calculations were performed using Quantum Espresso package [51]. A total of 114 atoms were considered in the unit cell where the K-points were optimized to 422 till the energy difference was less than 10^{-3}. The cut-off for work function is taken as 46 and the cut-off for charge is 320. Ultrasoft pseudopotentials were taken for all the element types.

RESULTS AND DISCUSSION

FT-IR spectroscopic studies: In the analysis of FT-IR spectrum (Fig. 1) the bands at 1436 cm^{-1} and 1406 cm^{-1} are the result of stretching of partial double bond of C=O bond of the oxalate ion. The O–H and N–H stretch are assigned to the peaks in the region around 3500-3300 cm^{-1}. The peaks at 2996 cm^{-1} and 2913 cm^{-1} correspond to the C–H stretch and the prominent peak at 1019 cm^{-1} is attributed to stretching of C–O single bond. The ^1H NMR spectrum (Fig. 2), where the shifts for the protons of the aromatic rings appear between 6.96 and 7.89 ppm. The peak at 5.36 ppm is the proton of the hydroxy group, while the peak at 3.76 corresponds to the hydrogens of the methoxy group. The ^{13}C NMR spectrum (Fig. 3) shows aromatic carbons in the range of 109.32 to 150.82 ppm. The downfield peak at 167.60 ppm is linked to the carbon atoms of the oxalate group, while the peak at 157.60 ppm corresponds

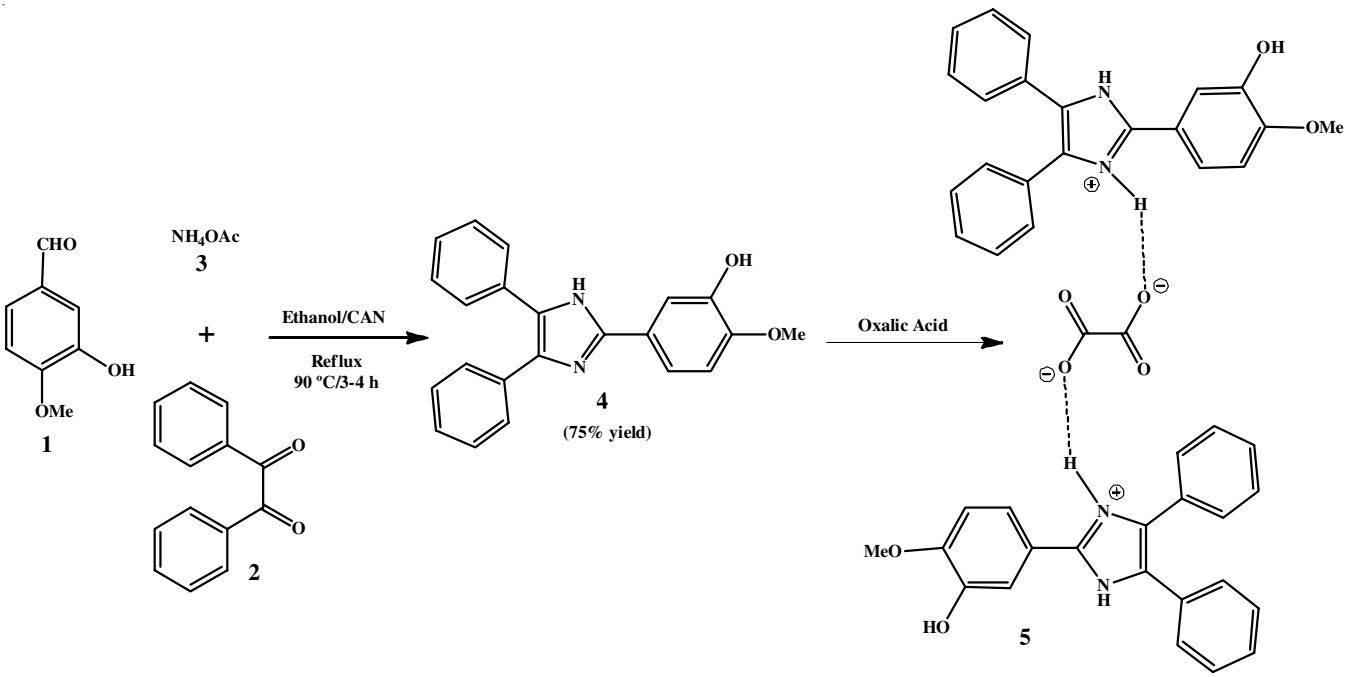

Scheme-I: Reaction scheme for the synthesis and crystal growth of imidazolium-oxalate co-crystal

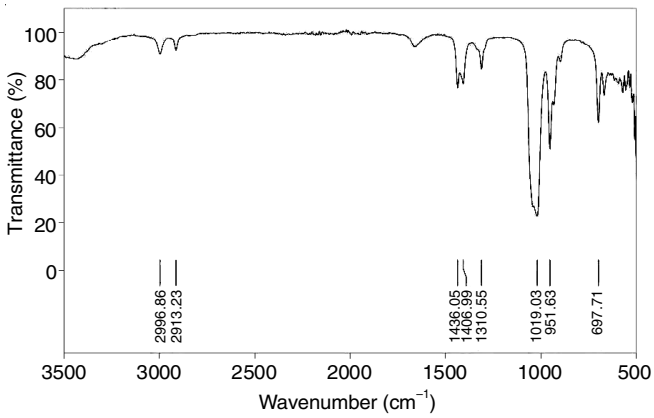

Fig. 1. IR spectrum of imidazole-oxalate co-crystal

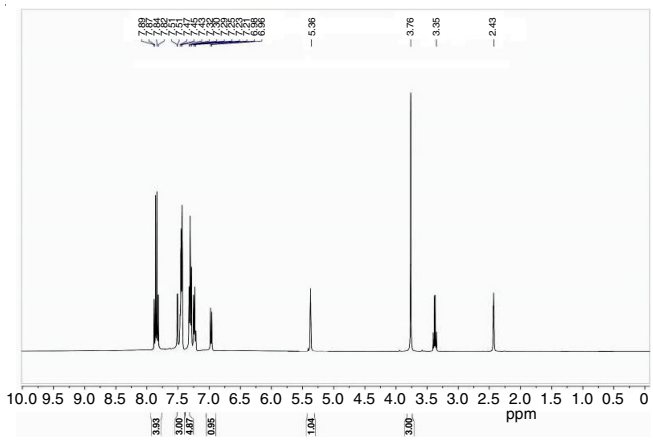

Fig. 2. ^{1}H NMR spectrum of imidazole-oxalate co-crystal

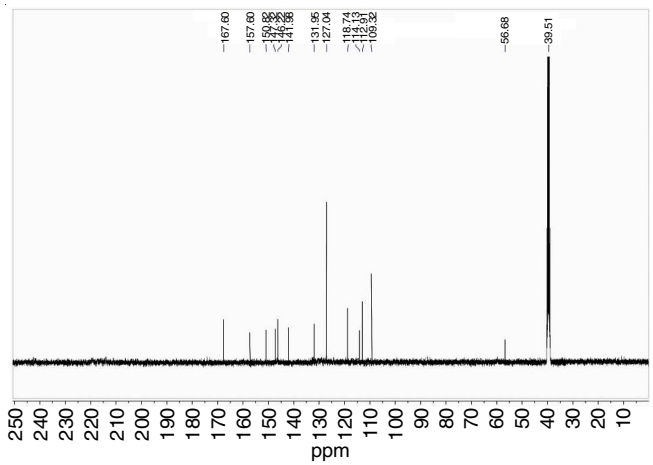

Fig. 3. ^{13}C NMR spectrum of imidazole-oxalate co-crystal

to carbon at second position of the imidazole ring and the peak at 56.68 ppm is related to the carbon of the methoxy group.

All the crystallographic information of the imidazolium-oxalate co-crystal is shown in Table-1, which summarizes all the details about the structure, data collection, refinement parameters and unit cell dimension. The crystal structure is available at Cambridge Crystallographic Data Centre with deposition ID as 2245588. The ortep representation of the crystal is illustrated in Fig. 4. The asymmetric unit of the crystal structure is given in Fig. 4a and the unit cell is shown in Fig. 4b. The

TABLE-1
CRYSTALLOGRAPHIC DATA OF
IMIDAZOLE-OXALATE CO-CRYSTAL

CCDC Number	2245588
Moiety formula	$2(C_{22}H_{19}N_2O_2)$, C_2O_4, $2(C_2H_6O)$
Temperature	296 K
Z	1
Formula weight	866.94 g/mol
Wavelength	0.71073 Å
Crystal system	Triclinic
Space group	P -1
Unit cell dimensions	a = 8.792(3); α = 82.881(9)
	b = 10.814(4) β = 75.347(9)
	c = 13.024(5) γ = 67.811(9)
Cell volume	1108.7(7) cm^3
Density	1.298 g/cm^3
F(000)	458
Theta range for data collection	2.017 - 29.624
Index ranges	$-11 \le h \le 11$, $-14 \le k \le 14$,
	$-17 \le l \le 17$
Reflections all	48975
Data completeness	0.985
Refinement method	Full-matrix least-squares
Data/restraints/parameters	5545/0/294
GOOF	1.025
Final R indices (I > 2sigma)	R1 = 0.0453, wR2 = 0.1138
R indices (all data)	R1 = 0.0609, wR2 = 0.1255

distances between the nitrogen donor and the oxygen acceptors from the oxalate and ethanol are measured at 2.7209(18) Å and 2.7206(18) Å, respectively, indicating the existence of the hydrogen bonding interactions between the protonated imidazolium moiety and both the oxalate ion and the solvent molecule. The unit cell is composed of two molecules of protonated imidazolium molecule, two solvent molecules and four oxalate ions.

As illustrated in Fig. 5, the interactions between the oxalate ions and the protonated imidazolium compound are evident. Each oxalate ion establishes hydrogen bonds with four molecules of protonated 5-(4,5-diphenyl-1*H*-imidazol-2-yl)-2-methoxy phenol, featuring N–H···O and O–H···O interactions.

Comparison of theoretical and experimental structure: The root mean square deviation and R^2 analysis were conducted to evaluate the correspondence between the theoretical structure with experimental structure. The various structural parameters of the experimental structure were derived from XRD data and subsequently compared with the structure of the constrained geometry optimization. The fragment of the structure selected for analysis, including atom labels and numbers, is presented in Fig. 6a. The image of constrained optimization with external frozen geometry is shown in Fig. 6b. Table-2 provides the correlation analyses results for the selected bond length and bond angle.

The correlation values for the bond lengths are calculated at 0.059 (RMSD) and 0.979 (R^2), respectively. The primary contributors to these deviations arise from are the N3-H4 and N6-H7 bond lengths. Overall, the bond length parameters of the optimized structure exhibit a strong correlation and minimal deviation from the experimental values. The optimized structure yields an RMSD of 1.188 and an R^2 correlation of 0.965,

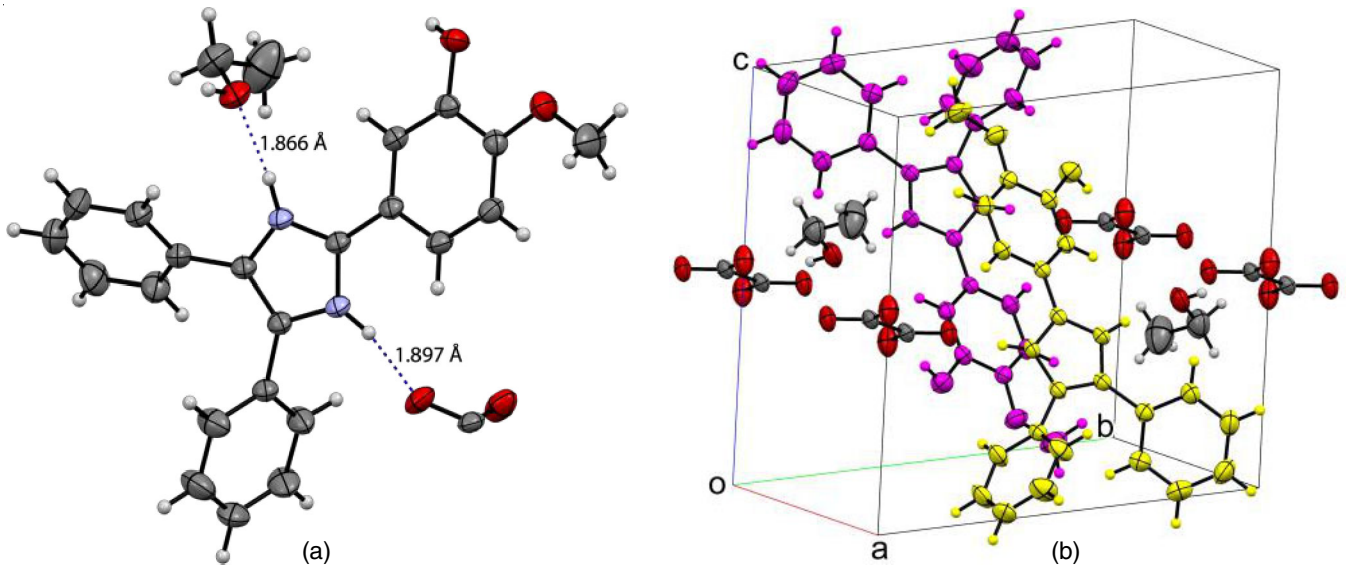

Fig. 4. Ortep view of imidazole-oxalate co-crystal. (a) Asymmetric unit with hydrogen bonding interaction. (b) Unit cell diagram imidazolium moiety coloured in magenta and yellow for clarity)

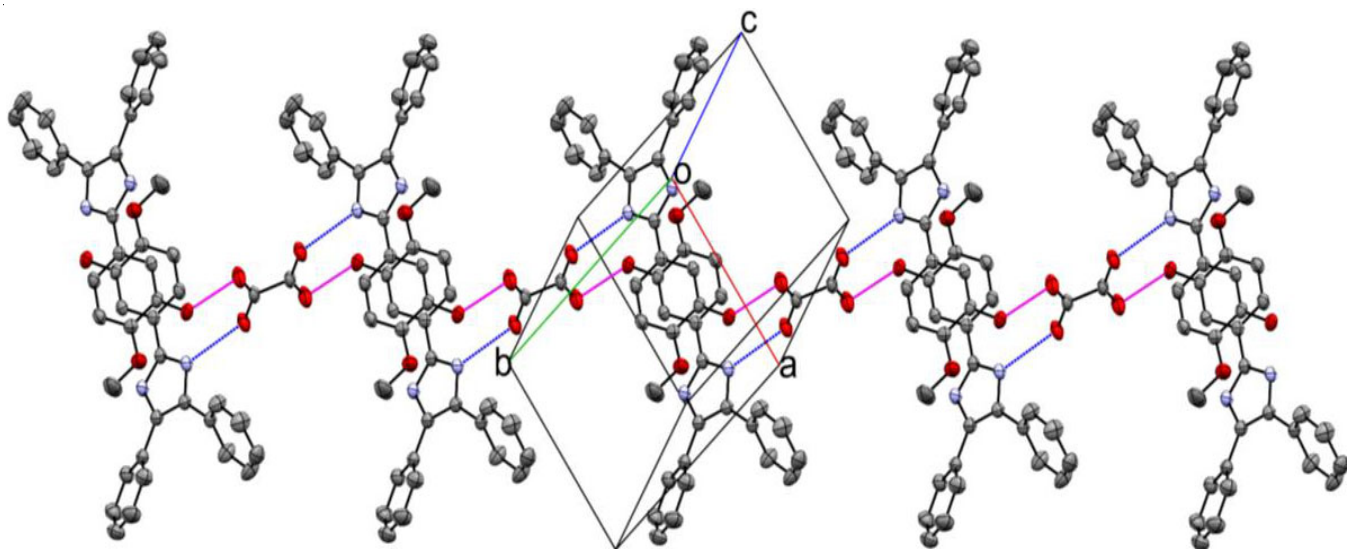

Fig. 5. Depictions of hydrogen bonding interactions in the imidazolium-oxalate co-crystal; (blue bonds) N–H···O interactions; (magenta bonds) O–H···O interactions. Hydrogen atoms and solvent molecules are omitted for clarity

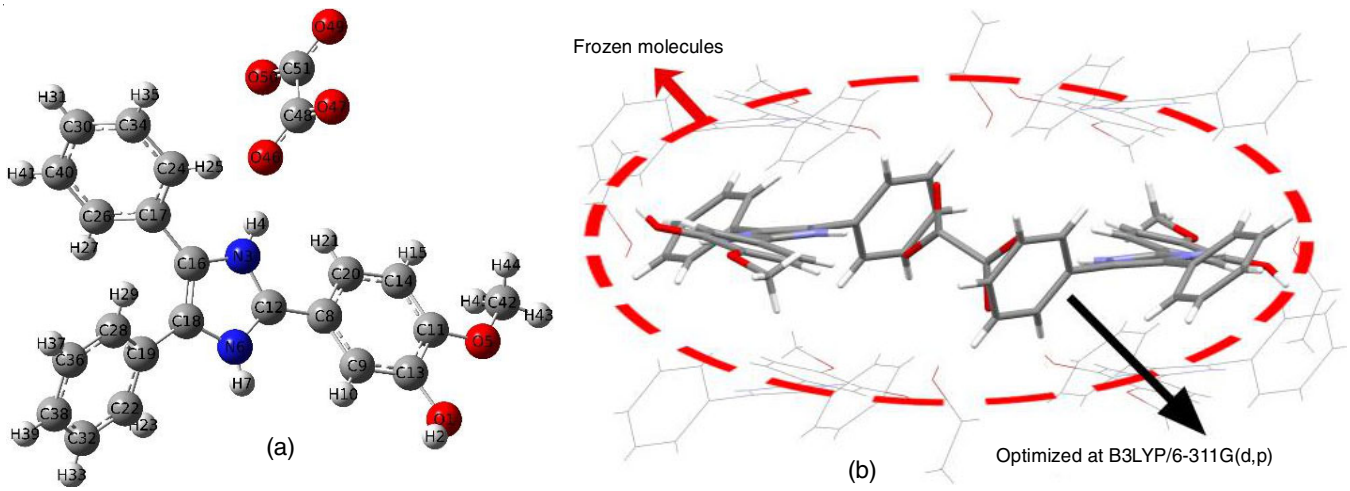

Fig. 6. Structure of imidazolium-oxalate co-crystal. (a) with atom labels (b) constrained optimized structure

TABLE-2
BOND LENGTH AND BOND ANGLE PARAMETERS FOR CORRELATION ANALYSIS

Bond length	XRD (Å)	Constrained phase (Å)	Bond angle	XRD (º)	Constrained phase (º)
N3-H4	0.860	1.0517	N3-C12-N6	106.98	105.23
N3-C12	1.343	1.3627	C12-N3-C16	109.82	111.08
N3-C16	1.381	1.3702	C12-N6-C18	110.15	110.59
C16-C18	1.365	1.3894	N6-C18-C16	106.17	104.91
N6-C18	1.388	1.4099	N3-C16-C18	106.85	108.05
N6-H7	0.860	1.0148	N3-C16-C17	122.35	121.14
N6-C12	1.335	1.3780	C24-C17-C26	119.20	119.38
C16-C17	1.476	1.4788	C24-C34-C30	120.78	120.672
C17-C24	1.385	1.4042	C26-C40-C30	119.78	119.92
C30-C34	1.374	1.3969	N6-C18-C19	122.80	122.44
C26-C40	1.381	1.3942	C22-C19-C28	118.45	116.60
C18-C19	1.471	1.4492	C28-C36-C38	119.88	121.26
C8-C12	1.459	1.4251	C22-C32-C38	120.57	120.87
C8-C20	1.386	1.4195	C9-C8-C20	119.20	117.03
C11-C14	1.380	1.4017	C11-C14-C20	120.39	121.31
C9-C13	1.385	1.3810	C9-C13-C11	119.49	121.12
O1-C13	1.349	1.3846	C11-O5-C42	117.16	117.13
O5-C11	1.366	1.3792	O1-C13-C9	124.35	122.11
O46-C48	1.239	1.2632	O46-C48-O47	126.82	127.05
C48-C51	1.564	1.5647	O49-C51-O50	126.82	127.04
RMSD		0.059	RMSD		1.188
R-squared		0.979	R-squared		0.965

indicating a close alignment between the optimized geometry and the reference geometry concerning variations in bond angles. Most of the bond angles in the optimized structure display only minor deviations, with no significant discrepancies observed in any specific angle under comparison. The correlation results for the dihedral parameters were obtained as 26.448 (RMSD) and 0.889 (R^2) as shown in Table-3. The deviations observed can be attributed to the dihedrals No.1, No.2, No.3 and No.4. Specifically, the deviations in No.1 and No.2 are caused by the rotation along the C8-C12 bond that connects the imidazole ring with the methoxyphenol ring. Also, the deviations in dihedrals No.3 and No.4 are due to the rotations around the C16-C17 and C18-C19 bonds, which serve to bridge the imidazole ring to the diphenyl rings.

TABLE-3
DIHEDRAL ANGLE PARAMETERS
FOR CORRELATION ANALYSIS

S. No.	Dihedral angle	XRD (º)	Constrained phase (º)
1	N3-C12-C8-C20	-19.67	-11.97
2	N6-C12-C8-C9	-19.55	-14.44
3	N3-C16-C17-C24	-58.62	-63.67
4	N6-C18-C19-C22	-37.25	-17.15
5	C17-C16-C18-C19	-1.29	1.64
6	O1-C13-C11-O5	0.36	4.68
7	O47-C48-C51-O49	-0.272	-0.49
8	O46-C48-C51-O50	0.272	0.44
	RMSD		26.44
	R-squared		0.889

Electrostatic potential surface: Molecular electrostatic potential (MEP) surface gives us a visual maps of the electrostatic potential around a molecule, indicating the positive and negative charge distribution which relates to potential reactive sites [52]. MEP surface can be used to interpret molecular electronic structure, reactivity and interactions of the molecule [53]. The surface is colour-coded, with red indicating nucleophilic regions, blue for electrophilic areas and green for neutral zones. Fig. 7 presents the MEP surface of the compound studied, where the surfaces around the oxalate ions are highly nucleophilic and the rest of the surfaces show slight electrophilic properties.

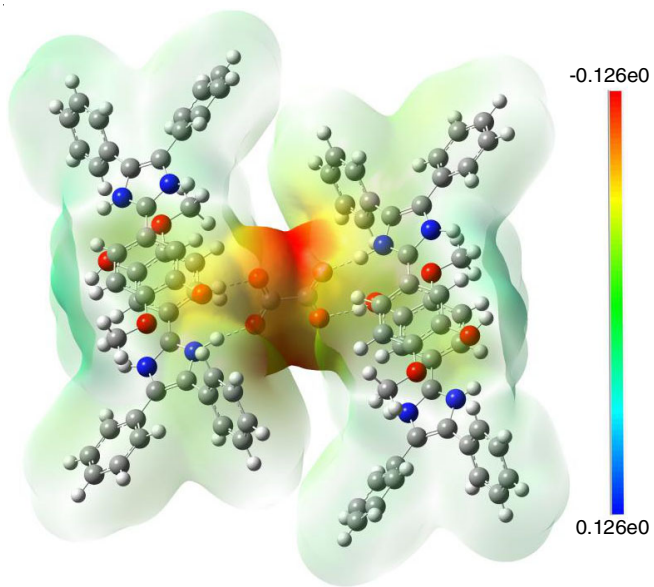

Fig. 7. MEP plot of imidazolium-oxalate co-crystal

Hirshfeld surface study: The Hirshfeld surface of the studied crystal is shown in Fig. 8. The red regions in Fig. 8a-b represents strong polar interactions between the protonated imidazolium molecule and the oxalate ion. The two pairs of spikes in the fingerprint plot (Fig. 9) confirms the presence of highly polar hydrogen bonding interaction involving the oxalate

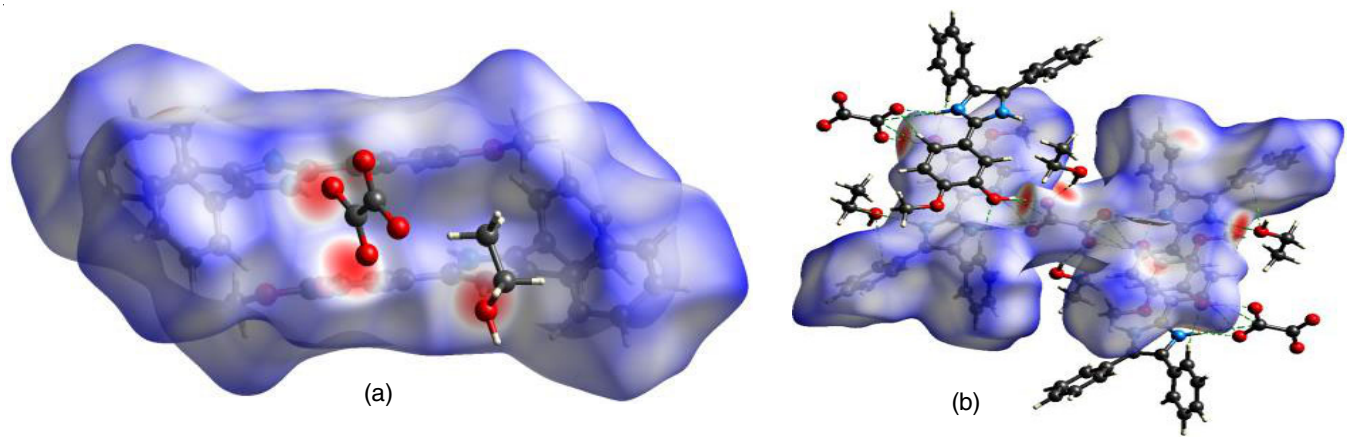

Fig. 8. Hirshfeld surface of imidazolium-oxalate co-crystal. (a) interactions of the oxalate ion and solvent molecule with two imidazolium molecules (b) hirsfeld surface chosen for fingerprint plot analysis

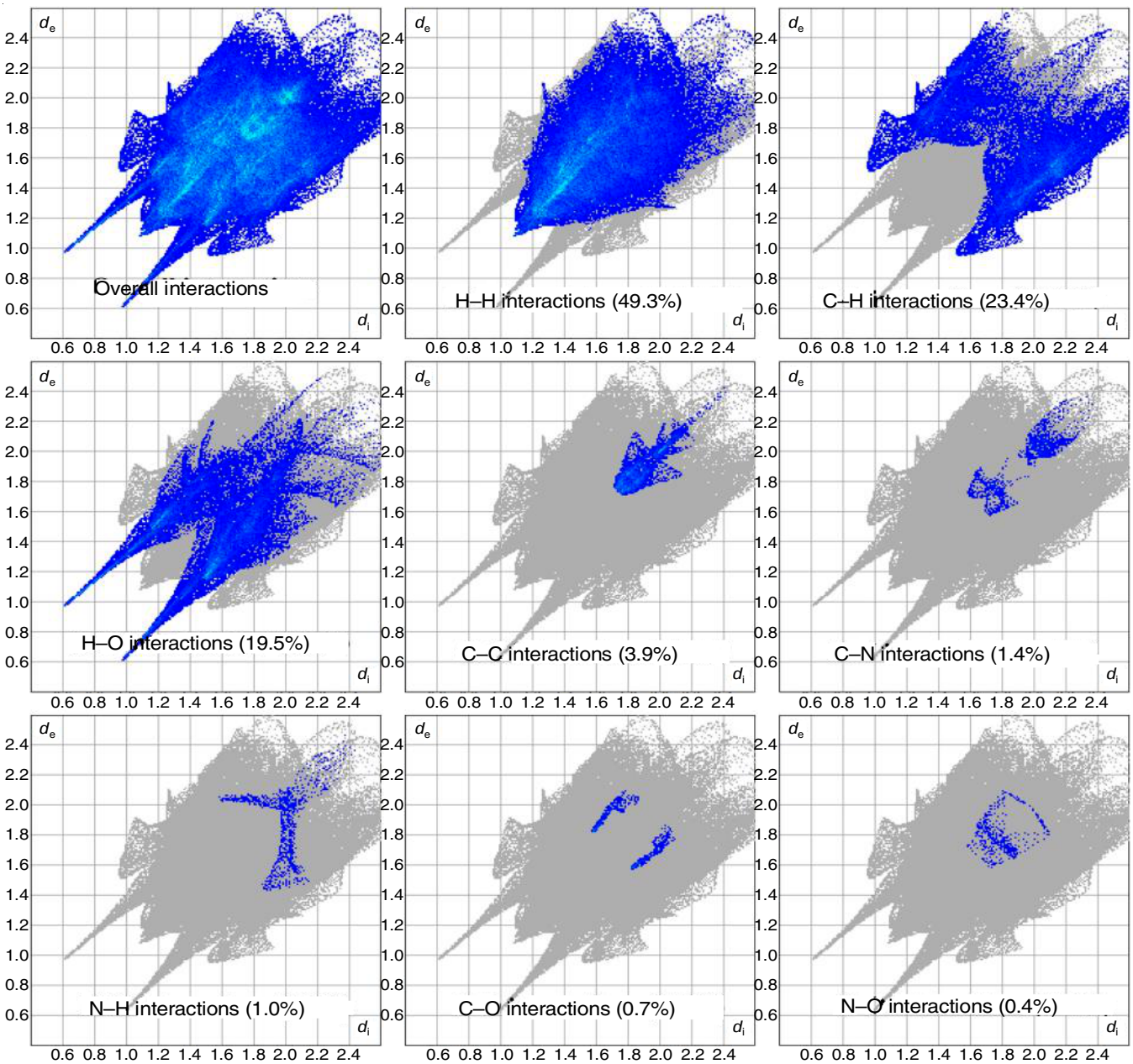

Fig. 9. Two-dimensional fingerprint plots of imidazolium-oxalate co-crystal

ion. Although there are aromatic rings in the structure there is no evidence of stacked π-interactions due to the absence of red regions in the middle of the fingerprint plot.

HOMO-LUMO analysis: The characteristics of the frontier molecular orbitals (FMOs) for the compound analyzed is illustrated in Fig. 10. FMOs were analyzed for the compound in liquid phase with ethanol as solvent. Charge localization at different regions in the frontier molecular orbitals indicates a potential for charge transfer among various moieties within the complex. In the LUMO charge density around the oxalate ions are missing, hence, a charge transfer from the oxalate ion of the HOMO was observed. The complex in the liquid state has an energy gap (ΔE) of 4.21 eV, indicating higher kinetic stability and lower reactivity [54].

Electronic transitions: The experimental and theoretical UV absorption spectrum of imidazole compound is compared in Fig. 11. After the normalization of absorbance value of the theoretical data, the theoretical spectrum has resemblance with the experimental spectrum. Based on the theoretical model, the spectrum consists of two major transitions from HOMO →

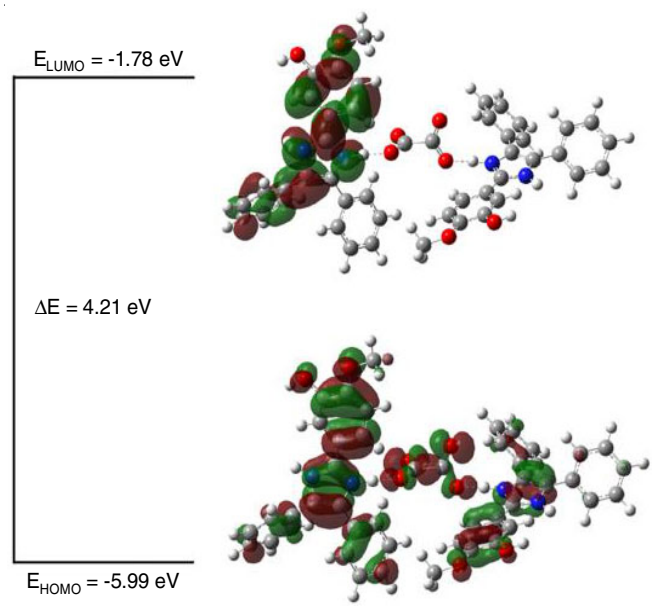

Fig. 10. HOMO-LUMO plots of imidazolium-oxalate co-crystal in ethanol

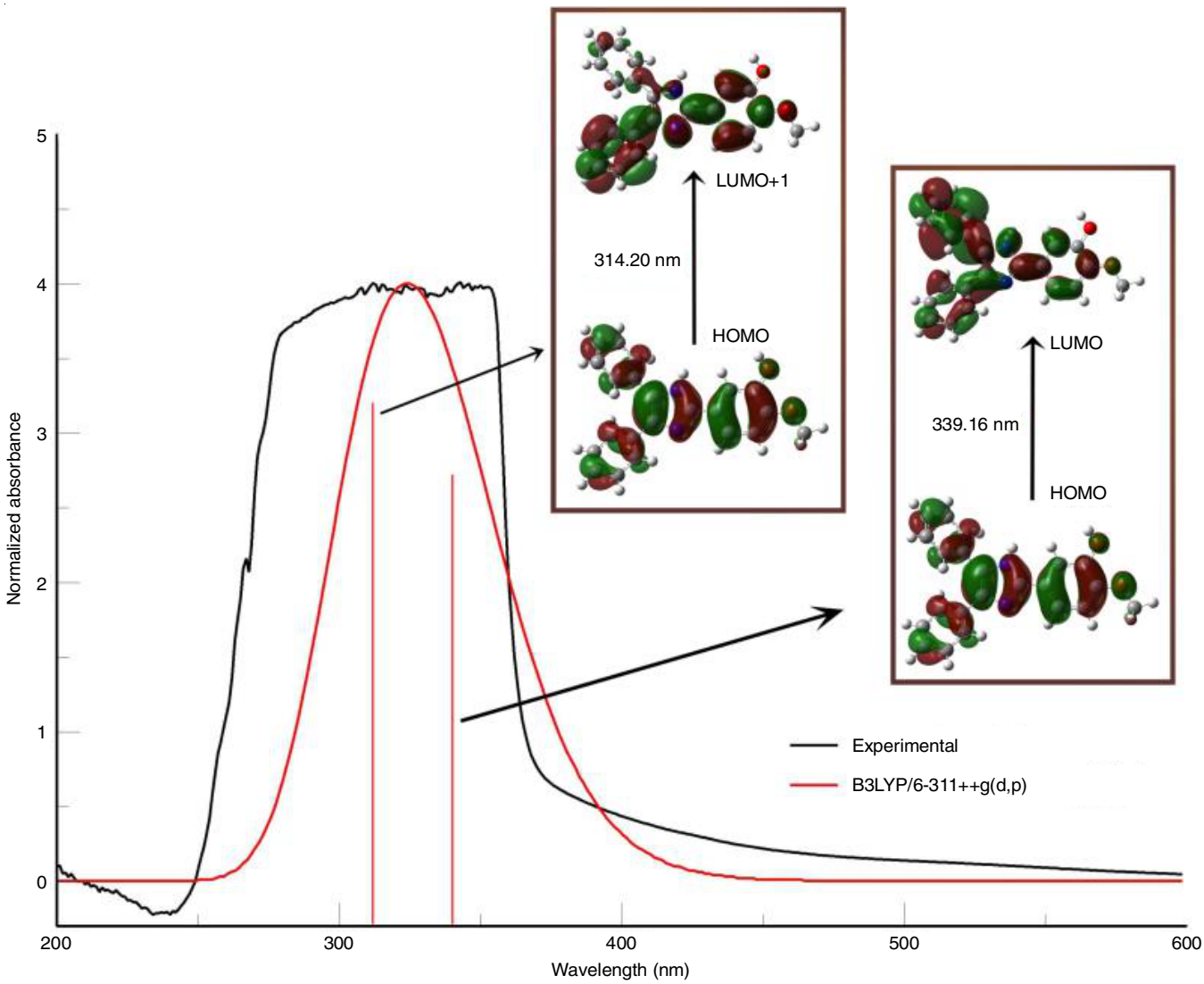

Fig. 11. UV-Visible spectra of imidazole derivative (compound **4**) (both experimental and theoretical)

LUMO+1 at 314.20 nm and from HOMO → LUMO at 339.16 nm. The corresponding oscillator frequency and the experimental wavelength of the peaks are given in Table-4.

The UV absorption spectrum of imidazole compound are shown in Fig. 12. Based on the theoretical spectrum, there is only a single major transition comprising of three different transitions to the LUMO at 329.02 nm. These transitions would involve the movement of charge densities from the oxalate to the imidazole groups as there is absence of charge densities around the oxalate in the LUMO. The designated experimental wavelength and the details of the allowed transitions are listed in Table-5. It can be concluded that the interaction with the oxalate ion reduces the energy gap among HOMO, HOMO-1 and HOMO-2, resulting in the formation of a single major transition comprising of all these three levels.

Band gap and density of states: The band gap value and the density of states are shown in Fig. 13. Unlike the solvent state, the solid state of imidazolium-oxalate co-crystal has a band gap (ΔE) value of 1.807 eV and can be investigated as organic semiconductor material [55-57]. The major contribution to the HOMO is coming from the oxalate moiety (red line), which corresponds to the TD-DFT studies where significant

TABLE-4
MAJOR ELECTRONIC TRANSITIONS OF IMIDAZOLE DERIVATIVE (COMPOUND **4**)

Energy (eV)	λ (nm) calculated	Oscillator frequency (*f*)	λ (nm) experimental	Orbital transitions
3.6557	339.16	0.4914	342.17	HOMO→LUMO
3.9460	314.20	0.6140	311.67	HOMO→LUMO+1

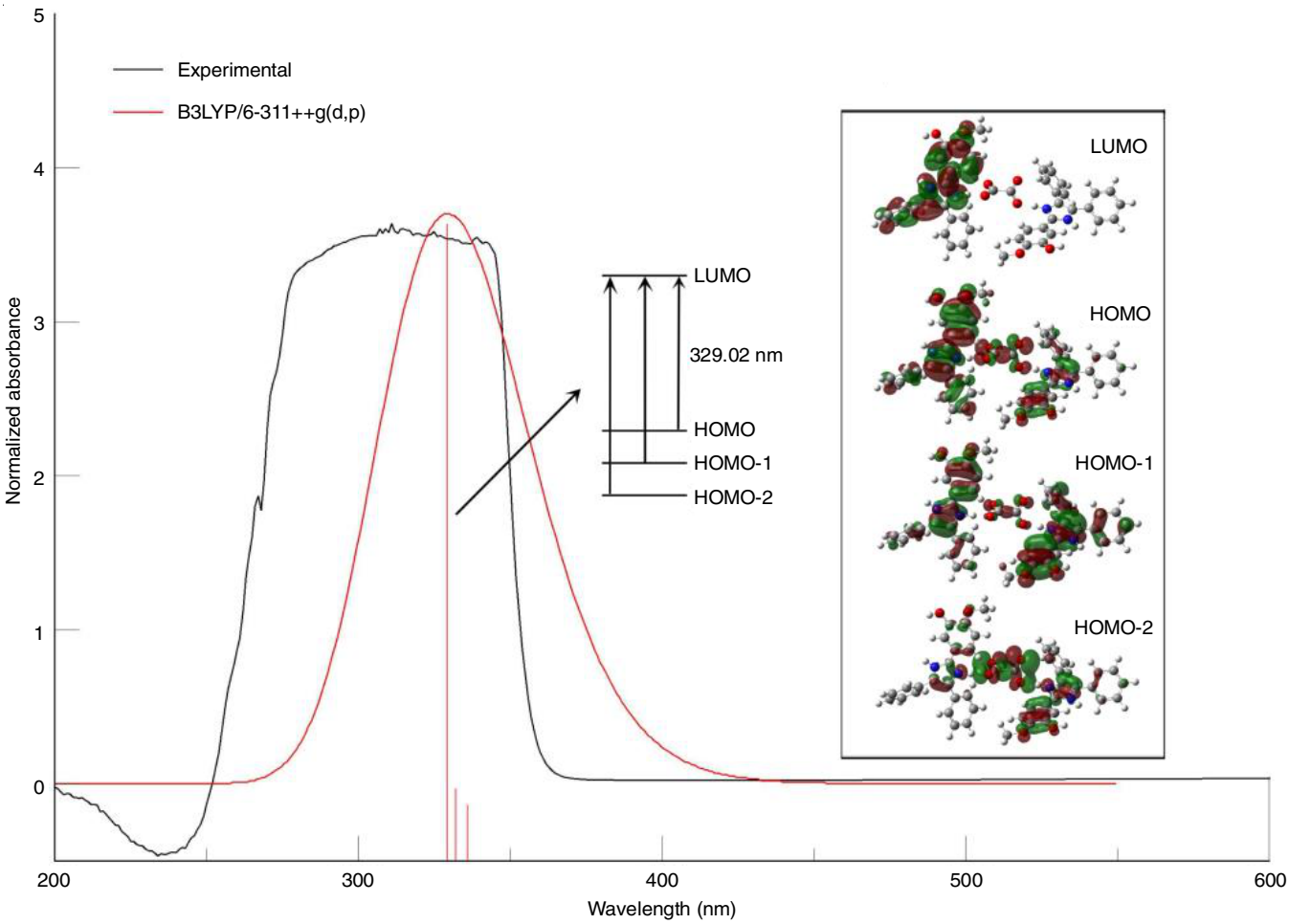

Fig. 12. UV-Visible spectra of imidazolium-oxalate co-crystal (both experimental and theoretical)

TABLE-5
MAJOR ELECTRONIC TRANSITIONS OF IMIDAZOLIUM-OXALATE CO-CRYSTAL

Energy (eV)	λ (nm) calculated	Oscillator frequency (*f*)	λ (nm) experimental	Orbital transitions
3.7076	334.23	0.0446	338.69	HOMO-2→LUMO; HOMO→LUMO
3.7422	331.31	0.0632	323.705	HOMO-2→LUMO+1; HOMO-1→LUMO+1; HOMO→LUMO+1
3.7683	329.02	0.7546	319.59	HOMO-2→LUMO; HOMO-1→LUMO; HOMO→LUMO

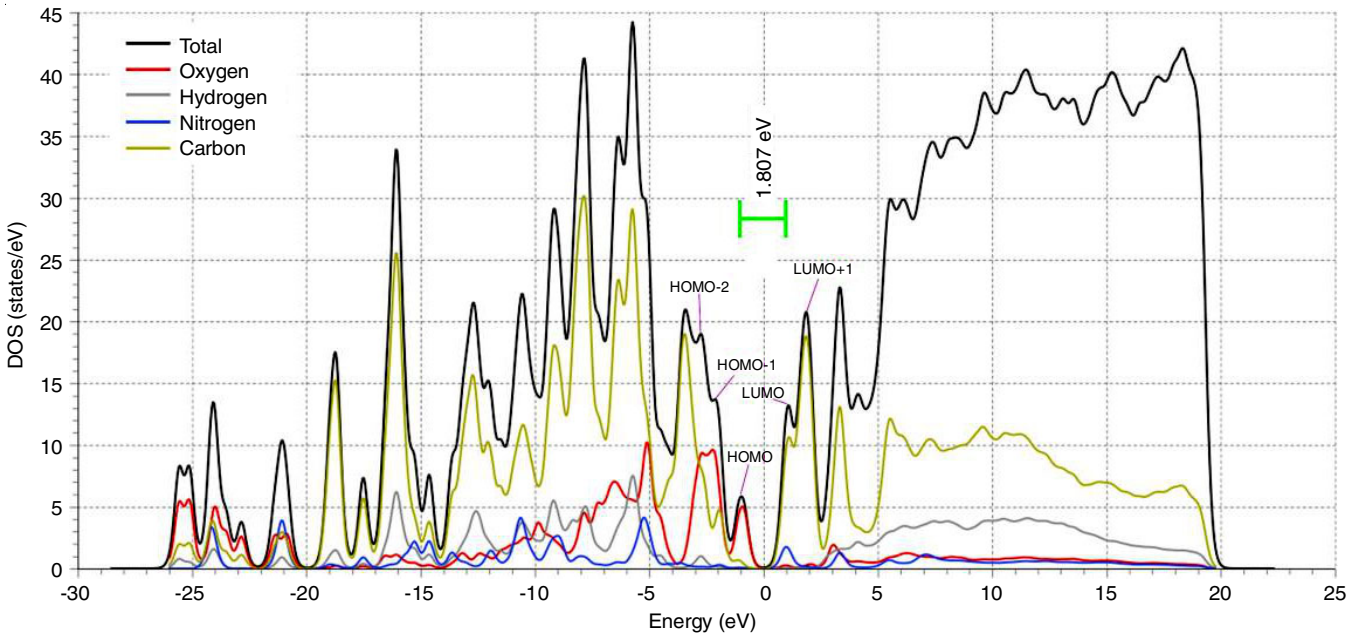

Fig. 13. Graphical representation of total density of states (TDOS) and the contribution from each elemental type

charge densities in the HOMO are located around the oxalate moiety. The higher charge densities in the HOMO-1 and HOMO-2 in the total density of states (black line) confirm the higher possibility of transitions from these states. The charge densities on LUMO and LUMO+1 are located in the phenyl rings in the imidazole compound (green lines) with is also confirm by TD-DFT studies (Fig. 12). The high charge densities on both LUMO and LUMO+1 (greens lines) also reaffirms the transitions to these states as given in Table-5.

Conclusion

A novel imidazolium-oxalate co-crystal was successfully synthesized and grown. Its structural characterization was performed utilizing various spectroscopic and XRD techniques. The structure reveals the protonation of the imidazole ring and deprotonation of oxalic acid. Investigations into polar bonding interactions, along with Hirshfeld surface analysis, indicate the presence of robust N–H···O and O–H···O hydrogen bonds, which contribute to the stabilization of the crystal structure. Furthermore, the root mean square deviation (RMSD) and R^2 correlation assessments demonstrate a strong correlation between the constrained optimized geometry and the experimental data. The UV-visible spectroscopy illuminated the optical behaviour of the compound and the various electronic structure and transitions have been studied. With the study of frontier molecular orbitals, coupled with TD-DFT and density of states studies, the authors recommends further investigation of the organic crystal in the field of organic semiconductor and opto-electronic materials.

ACKNOWLEDGEMENTS

The authors express their sincere gratitude to St. Joseph's College (A), Jakhama and St. Joseph University Chümoukedima for providing the necessary research facilities that facilitated the research. Furthermore, the authors wish to acknowledge SAIC, Tezpur University, India, for their assistance in obtaining high-quality single crystal XRD data.

CONFLICT OF INTEREST

The authors declare that there is no conflict of interests regarding the publication of this article.

REFERENCES

1. O. Ostroverkhova, *Chem. Rev.*, **116**, 13279 (2016); https://doi.org/10.1021/acs.chemrev.6b00127
2. Y.-L. Shi, M.-P. Zhuo, X.-D. Wang and L.-S. Liao, *ACS Appl. Nano Mater.*, **3**, 1080 (2020); https://doi.org/10.1021/acsanm.0c00131
3. P. Yu, Y. Zhen, H. Dong and W. Hu, *Chem*, **5**, 2814 (2019); https://doi.org/10.1016/j.chempr.2019.08.019
4. M. Jazbinsek, U. Puc, A. Abina and A. Zidansek, *Appl. Sci.*, **9**, 882 (2019); https://doi.org/10.3390/app9050882
5. X. Yang, B. Gao, Y. Liu, B. Tang, H. Zhang and H. Zhang, *J. Mater. Chem. C Mater.*, **13**, 6547 (2025); https://doi.org/10.1039/D5TC00112A
6. X. Yang, M.B. Al-Handawi, L. Li, P. Naumov and H. Zhang, *Chem. Sci.*, **15**, 2684 (2024); https://doi.org/10.1039/D3SC06469G
7. W. Wu, K. Chen, T. Wang, N. Wang, X. Huang, L. Zhou, Z. Wang and H. Hao, *J. Mater. Chem. C*, **11**, 2026 (2023); https://doi.org/10.1039/D2TC04642C
8. D. Liao, M. Li, J. Wang, M. Zhang, M. Qiu and C. An, *J. Mater. Res. Technol.*, **27**, 3098 (2023); https://doi.org/10.1016/j.jmrt.2023.10.146
9. X. Zhou, J. Shan, D. Chen and H. Li, *Crystals*, **9**, 392 (2019); https://doi.org/10.3390/cryst9080392.
10. L. Zhu and Y.-B. Zhang, *Molecules*, **22**, 1149 (2017); https://doi.org/10.3390/molecules22071149
11. M.E. Casco, F. Krupp, S. Grätz, A. Schwenger, V. Damakoudi, C. Richert, W. Frey and L. Borchardt, *Adsorption*, **26**, 1323 (2020); https://doi.org/10.1007/s10450-020-00259-8
12. R. Zhang, H. Daglar, C. Tang, P. Li, L. Feng, H. Han, G. Wu, B.N. Limketkai, Y. Wu, S. Yang, A.X.-Y. Chen, C.L. Stern, C.D. Malliakas, R.Q. Snurr and J.F. Stoddart, *Nat. Chem.*, **16**, 1982 (2024); https://doi.org/10.1038/s41557-024-01622-w

13. C. Graiff, *Crystals*, **10**, 1021 (2020); https://doi.org/10.3390/cryst10111021
14. N. Panina, F.J.J. Leusen, F.F.B.J. Janssen, P. Verwer, H. Meekes, E. Vlieg and G. Deroover, *J. Appl. Cryst.*, **40**, 105 (2007); https://doi.org/10.1107/S0021889806043767
15. L.S. Taylor, D.E. Braun and J.W. Steed, *Cryst. Growth Des.*, **21**, 1375 (2021); https://doi.org/10.1021/acs.cgd.0c01592
16. M. Baziar, H.R. Zakeri, S. Ghaleh askari, Z.D. Nejad, M. Shams, I. Anastopoulos, D.A. Giannakoudakis and E.C. Lima, *J. Mol. Liq.*, **332**, 115832 (2021); https://doi.org/10.1016/j.molliq.2021.115832
17. S. Liu, H. Li, Y. Shuai, Z. Ding and Y. Liu, *Mater. Adv.*, **3**, 8647 (2022); https://doi.org/10.1039/D2MA00580H
18. N. Motakef-Kazemi, F. Ataei and D. Dorranian, *Opt. Quantum Electron.*, **55**, 921 (2023); https://doi.org/10.1007/s11082-023-04775-z
19. A. Cammers and S. Parkin, *CrystEngComm*, **6**, 168 (2004); https://doi.org/10.1039/b405096g
20. J. Liu, X.-Y. Su, W.-H. Wang, Z.-H. Mao and R.-G. Xie, *Acta Crystallogr. Sect. E Struct. Rep. Online*, **62**, m1173 (2006); https://doi.org/10.1107/S1600536806014905
21. K.H. Asressu, C.-K. Chan and C.-C. Wang, *RSC Adv.*, **11**, 28061 (2021); https://doi.org/10.1039/D1RA05802A
22. T. Seethalakshmi, A. Puratchikody, D.E. Lynch, P. Kaliannan and S. Thamotharan, *Acta Crystallogr. Sect. E Struct. Rep. Online*, **62**, o2803 (2006); https://doi.org/10.1107/S160053680602109X
23. C. Rajnák, J. Titiš, O. Fuhr, M. Ruben and R. Boèa, *Polyhedron*, **123**, 122 (2017); https://doi.org/10.1016/j.poly.2016.11.009
24. J.-C. Geng, C.-H. Jiao, J.-M. Hao and G.-H. Cui, *Z. Naturforsch. B. J. Chem. Sci.*, **67**, 791 (2012); https://doi.org/10.5560/znb.2012-0158
25. R.T. Stibrany, H.J. Schugar and J.A. Potenza, *Acta Crystallogr. Sect. E Struct. Rep. Online*, **60**, o1648 (2004); https://doi.org/10.1107/S1600536804019555
26. T. Mohandas, R. Sathishkumar, J. Jayabharathi, A. Pasupathi and P. Sakthivel, *Acta Crystallogr. Sect. E Struct. Rep. Online*, **69**, o1293 (2013); https://doi.org/10.1107/S1600536813019351
27. T. Kavitha, S. Mayakrishnan, T.P. Perumal, C. Suvasini and S. Lakshmi, *IUCrdata*, **2**, x170089 (2017); https://doi.org/10.1107/S241431461700089X
28. A. Karak, S. Banerjee, S. Halder, M. Mandal, D. Banik, A. Maiti, K. Jana and A.K. Mahapatra, *New J. Chem.*, **47**, 16756 (2023); https://doi.org/10.1039/D3NJ02545D
29. W. Hao, Y. Wang, H. Zhao, J. Zhu and S. Li, *Phys. Chem. Chem. Phys.*, **22**, 13802 (2020); https://doi.org/10.1039/D0CP01520B
30. S. Sarkar, P.K. Sruthi, N. Ramanathan and K. Sundararajan, *J. Mol. Struct.*, **1204**, 127511 (2020); https://doi.org/10.1016/j.molstruc.2019.127511
31. Q. Zheng, X. Li, K. Kurpiewska and A. Dömling, *Org. Lett.*, **24**, 5014 (2022); https://doi.org/10.1021/acs.orglett.2c01642
32. R. Justin Grams, K. Yuan, M.W. Founds, M.L. Ware, M.G. Pilar and K. Hsu, *ChemBioChem*, **25**, e202400382 (2024); https://doi.org/10.1002/cbic.202400382
33. S.B. Akula, C. Su, Y.S. Tingare, H.-C. Lan, Y.-J. Lin, Y.-T. Wang, Y.-C. Jheng, X.-C. Lin, Y.-C. Chang and W.-R. Li, *J. Mater. Chem. C Mater. Opt. Electron. Devices*, **8**, 16577 (2020); https://doi.org/10.1039/D0TC03438J
34. A. Gabriel Tomulescu, L. Nicoleta Leonat, F. Neatu, V. Stancu, V. Toma, S. Derbali, S. Neatu, A. Mihai Rostas, C. Besleagã, R. Pãtru, I. Pintilie and M. Florea, *Sol. Energy Mater. Sol. Cells*, **227**, 111096 (2021); https://doi.org/10.1016/j.solmat.2021.111096
35. W. Pan, J. Lin, J. Wu, X. Wang, G. Li, Y. Du, W. Li, W. Sun and Z. Lan, *Appl. Surf. Sci.*, **604**, 154486 (2022); https://doi.org/10.1016/j.apsusc.2022.154486
36. M. Mamada, C. PérezBolívar, D. Kumaki, N.A. Esipenko, S. Tokito and P. Anzenbacher Jr., *Chem. Eur. J.*, **20**, 11835 (2014); https://doi.org/10.1002/chem.201403058
37. B.N. Bideh, M. Moghadam, A. Sousaraei and B.S. Arani, *Sci. Rep.*, **13**, 2287 (2023); https://doi.org/10.1038/s41598-023-29527-7
38. P. Solo and M. Arockia doss, *J. Chem. Crystallogr.*, **54**, 225 (2024); https://doi.org/10.1007/s10870-024-01016-3
39. P. Solo and M. Arockia doss, *Polycycl. Aromat. Compd.*, **43**, 4924 (2023); https://doi.org/10.1080/10406638.2022.2096650
40. P. Solo and M. Arockia doss, *J. Iranian Chem. Soc.*, **21**, 2907 (2024); https://doi.org/10.1007/s13738-024-03111-w
41. S.K. Callear, M.B. Hursthouse and T.L. Threlfall, *CrystEngComm*, **12**, 898 (2010); https://doi.org/10.1039/B917191F
42. A. Rachocki, K. Pogorzelec-Glaser and J. Tritt-Goc, *Appl. Magn. Reson.*, **34**, 163 (2008); https://doi.org/10.1007/s00723-008-0088-6
43. S. Priya and D.R. Babu, *J. Mol. Struct.*, **1291**, 135980 (2023); https://doi.org/10.1016/j.molstruc.2023.135980
44. J.N. Sangshetti, N.D. Kokare, S.A. Kotharkara and D.B. Shinde, *J. Chem. Sci.*, **120**, 463 (2008); https://doi.org/10.1007/s12039-008-0072-6.
45. G.M. Sheldrick, *Acta Crystallogr. A*, **64**, 112 (2008); https://doi.org/10.1107/S0108767307043930.
46. G.M. Sheldrick, *Acta Crystallogr. C Struct. Chem.*, **71**, 3 (2015); https://doi.org/10.1107/S2053229614024218
47. O.V. Dolomanov, L.J. Bourhis, R.J. Gildea, J.A.K. Howard and H. Puschmann, *J. Appl. Cryst.*, **42**, 339 (2009); https://doi.org/10.1107/S0021889808042726
48. M.J. Frisch, G.W. Trucks, H.B. Schlegel, G.E. Scuseria, M.A. Robb, J.R. Cheeseman, G. Scalmani, V. Barone, B. Mennucci, G.A. Petersson, H. Nakatsuji, M. Caricato, X. Li, H.P. Hratchian, A.F. Izmaylov, J. Bloino, G. Zheng, J.L. Sonnenberg, M. Hada, M. Ehara, K. Toyota, R. Fukuda, J. Hasegawa, M. Ishida, T. Nakajima, Y. Honda, O. Kitao, H. Nakai, T. Vreven, J.A. Montgomery Jr., J.E. Peralta, F. Ogliaro, M. Bearpark, J.J. Heyd, E. Brothers, K.N. Kudin, V.N. Staroverov, R. Kobayashi, J. Normand, K. Raghavachari, A. Rendell, J.C. Burant, S.S. Iyengar, J. Tomasi, M. Cossi, N. Rega, J.M. Millam, M. Klene, J.E. Knox, J.B. Cross, R.L. Martin, V. Bakken, J.A. Jaramillo, R. Gomperts, R.E. Stratmann, O. Yazyev, R. Cammi, C. Pomelli, J.W. Ochterski, A.J. Austin, K. Morokuma, V.G. Zakrzewski, G.A. Voth, P. Salvador, J.J. Dannenberg, S. Dapprich, A.D. Daniels, Ö. Farkas, J.B. Foresman, J.V. Ortiz, J. Cioslowski and D.J. Fox, Gaussian 09, Revision D.01 Gaussian, Inc., Wallingford CT (2013).
49. P.R. Spackman, M.J. Turner, J.J. McKinnon, S.K. Wolff, D.J. Grimwood, D. Jayatilaka and M.A. Spackman, *J. Appl. Cryst.*, **54**, 1006 (2021); https://doi.org/10.1107/S1600576721002910
50. J. Tomasi, B. Mennucci and R. Cammi, *Chem. Rev.*, **105**, 2999 (2005); https://doi.org/10.1021/cr9904009
51. P. Giannozzi, S. Baroni, N. Bonini, M. Calandra, R. Car, C. Cavazzoni, D. Ceresoli, G.L. Chiarotti, M. Cococcioni, I. Dabo, A. Dal Corso, S. de Gironcoli, S. Fabris, G. Fratesi, R. Gebauer, U. Gerstmann, C. Gougoussis, M. Lazzeri, L. Martin-Samos, N. Marzari, F. Mauri, R. Mazzarello, A. Kokalj, S. Paolini, A. Pasquarello, L. Paulatto, C. Sbraccia, S. Scandolo, G. Sclauzero, A.P. Seitsonen, A. Smogunov, P. Umari and R.M. Wentzcovitch, *J. Phys. Condens. Matter*, **21**, 395502 (2009); https://doi.org/10.1088/0953-8984/21/39/395502
52. S. Lakshminarayanan, V. Jeyasingh, K. Murugesan, N. Selvapalam and G. Dass, *J. Photochem. Photobiol.*, **6**, 100022 (2021); https://doi.org/10.1016/j.jpap.2021.100022
53. A.M. Köster, M. Leboeuf and D.R. Salahub, Molecular Electrostatic Potentials from Density Functional Theory, pp. 105–142 (1996).
54. J. Aihara, *J. Phys. Chem. A*, **103**, 7487 (1999); https://doi.org/10.1021/jp990092i
55. R. Scholz, Organic Semiconductors," Encyclopedia of Condensed Matter Physics, pp. 206–221 (2005).
56. Y. Wang, F. Silveri, M.K. Bayazit, Q. Ruan, Y. Li, J. Xie, C.R.A. Catlow and J. Tang, *Adv. Energy Mater.*, **8**, 1801084 (2018); https://doi.org/10.1002/aenm.201801084
57. J.C.S. Costa, R.J.S. Taveira, C.F.R.A.C. Lima, A. Mendes and L.M.N.B.F. Santos, *Opt. Mater.*, **58**, 51 (2016); https://doi.org/10.1016/j.optmat.2016.03.041